


# Rotational separation after temporary coalescence in binary droplet collisions

Kuo-Long Pan <sup>\*</sup>, Kuan-Ling Huang, Wan-Ting Hsieh, and Chi-Ru Lu

*Department of Mechanical Engineering, National Taiwan University, Taipei 10617, Taiwan, Republic of China*



(Received 18 October 2018; published 2 December 2019)

Collision between two droplets plays a critical role in a wide range of processes, including raindrop formation, nuclear reactions, atomization and spraying in combustors, and various cooling, coating, and painting techniques. It is known that when two droplets collide nearly head-on, they may coalesce temporarily and then separate when the impact energy is so large that the rebounding motions of internal flows tend to stretch out and break the merged droplets. If the impact is sufficiently off-center, however, two distinct mechanisms have been argued to cause breakup exclusively. That is, separation has been reported to occur above a threshold of increasing impact angle (as characterized by an impact parameter,  $B$ ), due to either stretching or rotational dynamics, whereas only one of them is supposed to cause the transition from permanent coalescence to separation. Therefore, which one renders the sole mechanism leading to off-center separation is not clear in the literature. This has been a discrepancy in the past decades, considering the fact that both mechanisms have been used, respectively, in different studies to interpret and analyze the transition criteria. To resolve this ambiguity, here we demonstrate experimentally a new regime, named rotational separation, which is governed by the coupling of outer rotating flow and center rebounding flow in the tentatively united drops. This regime occurs at an intermediate  $B$ , in contrast to that dominated by stretching kinetics created at a slightly larger  $B$ . It thus indicates simultaneous existence of the two regimes but in different range on a phase diagram. Along with numerical simulations and physical models, we elucidate the two scenarios of off-center separations comprehensively and solve the long-standing puzzle.

DOI: [10.1103/PhysRevFluids.4.123602](https://doi.org/10.1103/PhysRevFluids.4.123602)

## I. INTRODUCTION

Collision between two droplets is an important element in fluid dynamic subjects including, e.g., formation of raindrops [1], operation of nuclear reactors [2,3], spray combustion in liquid-fueled combustors [4], firefighting via liquid injection [5], and various applications of spraying processes such as painting, coating, and cooling. The studies in the past decades have unveiled the basic structures and mechanisms leading to various outcomes after collisions between two droplets. Typically, they can coalesce, rebound, and temporarily coalesce followed by separation, concomitant with a few daughter droplets [6], or immediate splattering into many satellite droplets from the rim of an ejected lamella [1,7]. Based on two key parameters, the behaviours can be classified in a phase diagram indicative of the typical regimes from I to V [8], as shown in Fig. 1. The relative importance of inertia and surface tension is described by the Weber number,  $We = \rho U^2 D / \sigma$ , where  $U$  is the relative velocity of droplets,  $D$  the diameter, and  $\rho$  and  $\sigma$  respectively the density and surface tension. The effect of colliding angle is given by the impact parameter,  $B = \chi / D$ , where  $\chi$  is the projection of the separation distance between the droplet centers in the

<sup>\*</sup>Corresponding author: [panpeter@ntu.edu.tw](mailto:panpeter@ntu.edu.tw)

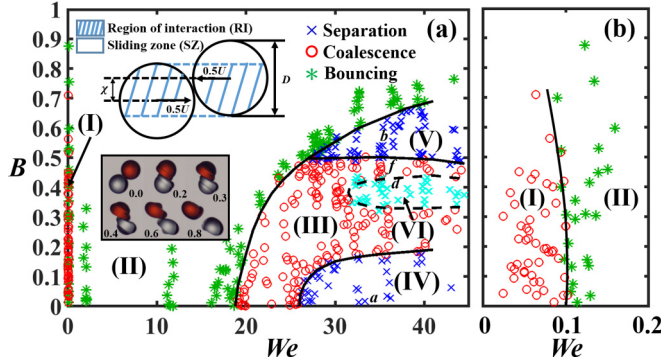


FIG. 1. (a) A regime diagram is summarized in terms of  $We$  and  $B$  using the present experimental results of dodecane at 1 atm ( $Oh = 0.0126$ ,  $D = 0.6$  mm). The inset presents the sequence of bouncing between two impinging droplets (one dyed in red) with time being expressed in millisecond ( $We = 34.78$ ,  $B = 0.704$ ). (b) An enlarged view of the transition between (I) and (II). As a general regime diagram for various liquids [8], (I) and (III) indicate permanent coalescence, (II) refers to bouncing, (IV) designates reflexive separation, and (V) indicates stretching separation (the latter two named by Ref. [12]). The regime indicating substantial breakup and splattering into many satellite droplets from the rim of an ejected disk at early stage [7] is created at much higher  $We$  and not included herein. The newly identified regime of rotational separation is designated as (VI), whose boundary is delineated by a dash line. The symbols:  $\circ$ , coalescence;  $\times$ , stretching/reflexive separation;  $*$ , bouncing;  $\times$ , rotational separation. The impact geometry with corresponding parameters are illustrated in the schematic.

direction normal to the relative velocity vector  $\mathbf{U}$ . Thus  $B = 0$  indicates head-on collision and  $B = 1$  designates glancing impact.

When  $We$  is sufficiently large, there is high possibility for droplets to coalesce temporarily and separate afterwards, tending to create more daughter droplets when  $We$  becomes larger. As shown in Fig. 2(a) for reflexive separation which is generated at a small  $B$ , i.e., in regime IV, breaking is resulted from the rebounding motions of the droplets when the impact is nearly head-on. The scenario can be understood unambiguously throughout the entire process that shows flattening and elongation followed by separation of the temporarily united drops.

For collisions at sufficiently high  $B$ , however, two different mechanisms have been reported to be responsible exclusively for the off-center separation, as referred to regime V. On the one hand, based on experimental observations of rotational motions after coalescence of two water droplets, a criterion for onset of ensuing disruption is given by balancing surface tension force and angular momentum [6] or via an evaluation of the rotational energy against surface energy [9] with increasing  $B$ . Similar accounts based on the angular velocity or centrifugal forces are reported in Refs. [10,11]. While the theoretical treatments of these studies appear to differ from each other, the dominating mechanisms have been assumed essentially to correlate with rotational dynamics.

On the other hand, in Ref. [12], stretching mechanics was claimed to take over the breaking before significant rotational motion could be observed. Specifically, the temporarily merged droplets separated soon due to inertia of the sliding zone [SZ, the part on the flanks without direct impact, as illustrated in Fig. 1(a)] that tended to shear off the colliding masses out of the region of interaction at the center (RI, the hatched area). This process is reproduced in the present experiment, as shown in Fig. 2(b). Therefore, a regime of stretching separation was identified when  $B$  became sufficiently large, in contrast to the formation of reflexive separation [Fig. 2(a)] due to internal rebounding motions of the impinging flows after merging in nearly head-on collisions. Many studies were conducted along this line to identify the mechanism and the boundary of transformation [13,14]. Nonetheless, the experimental images of Ref. [8] indicated significant motions of rotation after merging of two tetradecane droplets colliding at a high  $B$  that was supposed to fall in the regime of

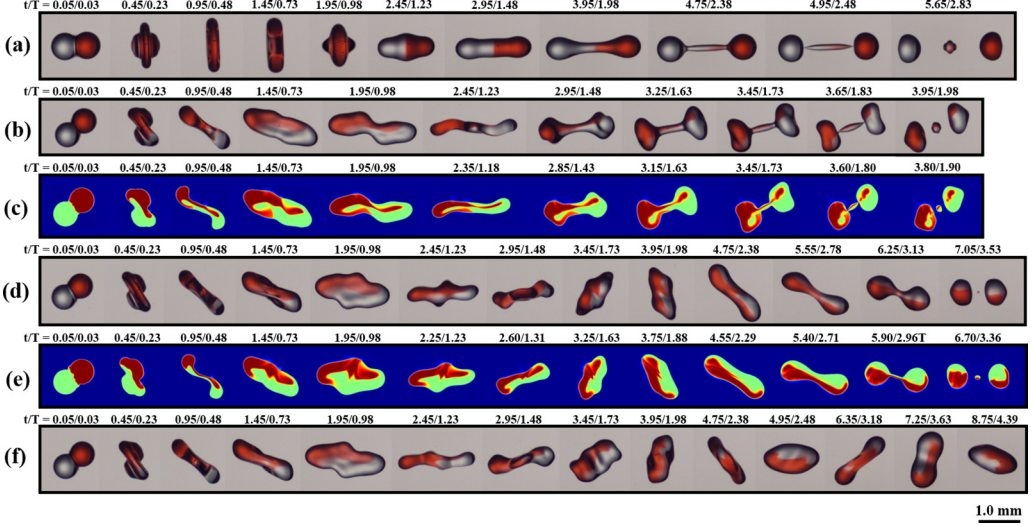


FIG. 2. The sequences of experiments for dodecane droplets (one dyed in red) at 1 atm ( $Oh = 0.0126$ ,  $D = 0.6$  mm) present (a) reflexive separation ( $We = 33.60$ ,  $B = 0.002$ ), (b) stretching separation ( $We = 35.04$ ,  $B = 0.547$ ), (c) 3D VOF simulation of (b) showing the mass distribution in the symmetry plane of computation, (d) rotational separation ( $We = 35.40$ ,  $B = 0.420$ ), (e) 3D simulation of (d) showing the mass distribution in the symmetry plane of computation, and (f) coalescence in the range of  $B$  between that of (V) and (VI) ( $We = 35.13$ ,  $B = 0.470$ ). The time is expressed both in millisecond and  $T = \frac{\pi}{4} \sqrt{\frac{\rho D^3}{\sigma}}$ . The corresponding locations of the cases on the regime diagram are marked in Fig. 1(a).

stretching separation. Though being distinct from that of Ref. [12], this observation was consistent with the analyses of earlier studies in Refs. [6,9] for water droplets. An ostensible difference in the two patterns was the occurrence of considerable rotation over  $180^\circ$  in the latter, whereas stretching separation was generated soon after impact without noticeable rotation. Based on the two distinctive mechanisms, different models have been proposed, leading to pronounced variations in the transition boundaries, as compared in Ref. [12] for several inviscid theories.

These seemingly contradictory results have given two disparate ways for understanding the scenarios of off-center collisions, which have puzzled researchers in the decades. The subsequent studies have mostly sorted the regime of off-center separation (V) to stretching separation, characterized by a transition boundary against the regime of coalescence (III) formed at lower  $B$ . But this obviously raises a question regarding how to interpret the rotational motions as observed by the others [6,8] on causing breakup of the united drops. The problem can be solved by the present finding in that, the regime exhibiting substantial rotations of merged drops, as shown in Fig. 2(d), is actually formed exclusively in a separate zone with  $B$  slightly smaller than that of stretching separation, for various liquids tested [Fig. 1(a)]. This regime is hence categorized as rotational separation, regime VI, while (V) is now referred unambiguously to stretching separation only.

In view of the remarkable discrepancy and significance of the governing mechanisms in related studies of various fields [13–22], the present work provides comprehensive interpretation and a model to elucidate the physical behaviors while taking into account both effects of surface tension and viscosity.

## II. EXPERIMENTAL APPROACH AND OBSERVATION

To collect a large number of data for delineating precisely the regimes of various collision outcomes, we have adopted a conventional drop-on-demand technique for generating droplets at

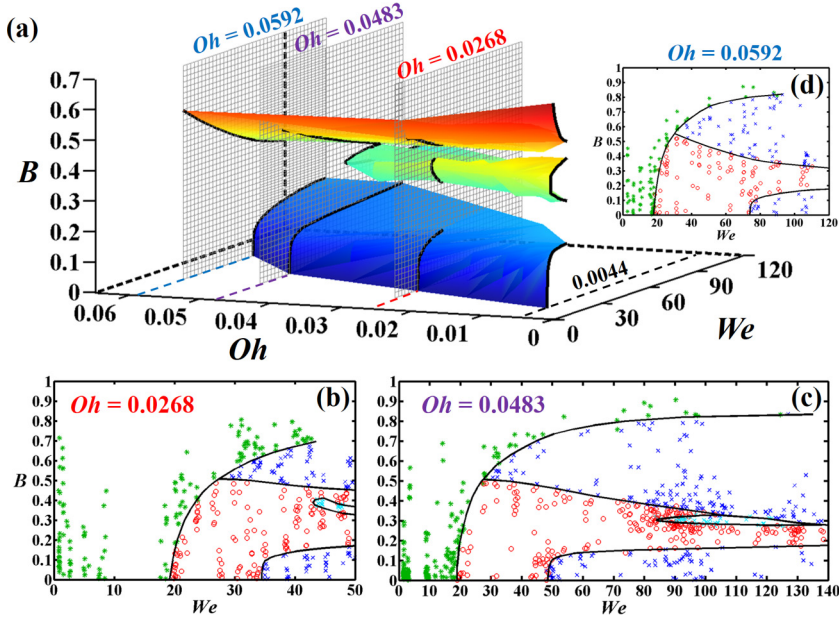


FIG. 3. (a) 3D plot of regimes IV, V, and VI in terms of  $We$ ,  $Oh$ , and  $B$ . The results of three cases, i.e.,  $Oh = 0.0268$ ,  $0.0483$ , and  $0.0592$ , are shown in (b)–(d), respectively. Here  $Oh$  ranges from  $0.0044$  to  $0.0592$ ; the test samples and conditions can be seen in Appendix A. The 3D surfaces in (a) are simply constructed from the 2D curves for assisting visualization and the colors do not refer to any physical meanings.

desired  $We$  and  $B$  with high accuracy [23]. Two identical droplets were generated by nozzles that were driven by vibrations of piezoelectric plates. They were made to impinge onto each other with adjusted angles of the colliding path. To enhance the precision of measurements, in particular, it is noticed that determination of the regime boundaries for off-center collisions is quite sensitive to the exact colliding conditions such as the impact angle. Significant uncertainty would be created if the collision is not formed completely in the plane of visualization normal to the camera recording direction. Therefore, another CCD camera was used on top to record the events and ensure that all collisions happened in the same plane. This can reduce errors due to three-dimensional (3D) out-of-plane effects, specifically on determination of the impact parameter, and hence dispersion of data around the boundaries which may lead to misjudgment of the outcome. A variety of liquids including water, various hydrocarbons, and silicone oil have been tested. More details and demonstrations are provided in Appendix A.

As shown in Fig. 3, different Ohnesorge numbers,  $Oh = \mu / \sqrt{\rho D \sigma}$ , where  $\mu$  is liquid viscosity, have rendered dramatic variations of the regimes, specifically regarding separation following temporary coalescence at sufficiently high  $We$ . Compared to Fig. 1(a), increasing  $Oh$  tends to narrow down and delay the onset of regime VI [Figs. 3(b) and 3(c)], revealing the impeding effect of viscous force on breaking of the coalesced droplets. Moreover, due to the increase of the transitional  $We$  of (VI) with higher  $Oh$ , the downward side of the expanding boundary of regime V with increasing  $We$  tends to cover up (VI), and eventually the regime of rotational separation is not observed in the available range of experiment [Fig. 3(d),  $Oh = 0.0592$ ]. This tendency signifies the significance of liquid viscosity in the formation of droplet breakup, and hence  $Oh$ , in addition to  $We$  and  $B$ . In this study, different liquids and droplet sizes have been tested and the regime diagram is presented in a general manner in terms of these key parameters.

Identical to previous studies [6,8,12,24], as  $B$  is close to zero, reflexive separation is observed, during which rebounding motions of the impinging flows lead to elongation of the temporarily



merged droplets and breakup in the end when a dumbbell shape is formed. When  $B$  is increased, the reflexive action becomes weaker due to reduced masses in RI and increasing off-center motions. The degenerate reflective flow eventually cannot overcome the restraining force of surface tension as  $B$  is above a threshold. Thence separation ceases to occur and permanent coalescence is resulted; the regime changes from IV to III.

For various liquids when  $B$  is sufficiently large and  $Oh < 0.0592$ , as seen in Fig. 3, two regimes of off-center separations are clearly demarcated, intervened by a band of coalescence (III). While the breadth of the intervening band varies with  $Oh$  and could be missed easily due to its narrowness and uncertainty of measurements, the characteristics of breakup patterns above and below this regime of coalescence are remarkably different. Specifically, as shown in Fig. 2(b) for (V), with substantial inertia in the original colliding course, the droplets stretch against each other during the tentative coalescence and break up shortly ( $t \sim 3.65 \text{ ms}/1.83 T$ ).

When  $B$  decreases [0.470, Fig. 2(f)], due to enlarged contact area between the droplets and increased surface force as well as decrease of masses in SZ of the merged droplets, the stretching parts cannot overcome the restraining surface tension and are dragged back toward RI; it leads to permanent coalescence. Moreover, the liquids in SZ pulled back by surface forces rotate around the center of mass (CM), as demonstrated by the two regions tagged with different colors of the distinct droplets. With further decrease in  $B$  [0.420, Fig. 2(d)], however, the masses drawn by the surface forces rotate against each other, leading to a state exhibiting a dumbbell shape ( $t = 5.55\text{--}6.25 \text{ ms}$ ). This occurs after a ligament is formed during the second elongation of oscillating cycles ( $\sim t = 3.95 \text{ ms}$ ), and the resulted neck eventually breaks ( $t = 7.05 \text{ ms}/3.53 T$ ). Compared to Fig. 2(b), undoubtedly, this separation occurs after a much longer period (about doubled time, as manifested in dimensionless time that is expressed in the unit of natural oscillation period,  $T$ ) with substantial rotation. This is distinct from the known scenarios of reflexive separation and stretching separation which are created, respectively, in near head-on and significantly off-center regimes. Their different features can be further appreciated in the Supplemental Material movies [25].

These facts clearly demonstrate the existence of a previously unidentified regime of separation following temporary merging of two droplets. This regime exhibiting remarkable rotation is close to but separate from the previously identified regime of off-center, stretching separation which has a much larger territory spanned over higher  $B$  area [Fig. 1(a) and Figs. 3(a)–3(c)].

### III. NUMERICAL SIMULATION

It is seen from the experimental images, in this regime VI, there is noticeable mass exchange during the process, as revealed from the variation of dyed area within the droplets. To quantify this transfer of mass and analyze the internal fluid motions, we have carried out numerical simulations for two-phase fluid dynamics. The computational approach is performed by using the volume-of-fluid (VOF) method provided by the open source Gerris code [17]. Descriptions including a convergence test and a validation of the simulation method are given in the following. The results of 3D simulations have shown incredible agreement with those of experiments.

#### A. Computational specifications and validation

The computational domain of the GERRIS 3D simulation is shown in Fig. 4(a), where the centers of two identical droplets with radius  $R = 0.3 \text{ mm}$  are placed in the symmetry plane. The initial velocity of each droplet is  $U/2$  but in opposite directions, and the distance between the centers of the droplets projected onto the plane perpendicular to the relative velocity vector is designated as  $\chi$ . In addition to the symmetry plane as indicated in the domain, the computational boundaries are set to have zero gradients for velocities, i.e., Neumann conditions, and fixed pressure at zero, i.e. Dirichlet conditions. The adaptive mesh refinement (AMR), with three different mesh sizes ( $\Delta_{\max}$ ,  $\Delta_{\text{mid}}$ ,  $\Delta_{\min}$ ), are performed in the computation to facilitate numerical simulation, where  $\Delta_{\max}$  is set in the gas phase,  $\Delta_{\min}$  in the liquid phase, and  $\Delta_{\text{mid}}$  in the high vorticity region of gas phase, as

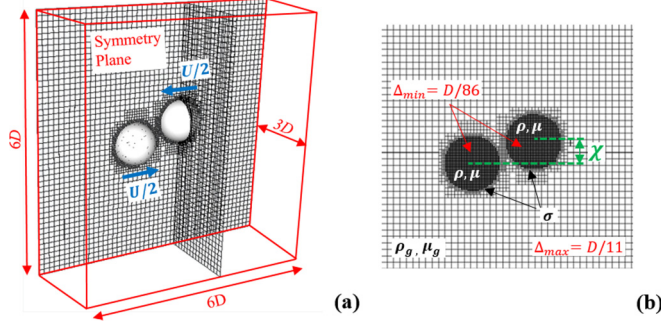


FIG. 4. (a) The schematic of computational domain and (b) the setting of adaptive meshes in the symmetry plane.

shown in Fig 4(b). By using the physical parameters listed in Table I and CFL number equal to 0.4, the experimental results ( $We = \rho U^2 D / \sigma$ ,  $B = \chi / D$ , and  $Oh = \mu / \sqrt{\rho D \sigma}$ ) can be reproduced by the simulations with the same impact conditions.

A test on the mesh dependency is carried out by implementing three numerical cases with the AMR level of  $(6D/2^6, 6D/2^7, 6D/2^8)$ ,  $(6D/2^6, 6D/2^7, 6D/2^9)$ , and  $(6D/2^6, 6D/2^7, 6D/2^{10})$ ; the results are shown in Figs. 5(b)–5(d), respectively. These cases all demonstrate stretching separation with one satellite droplet formed between two primary drops, which are consistent with the collision outcome shown in Fig. 5(a). To track the fluid motions in different drops, furthermore, two sets of passive tracers are allocated in the droplets, respectively. Since the liquid distribution and droplet deformation as shown in Figs. 5(c) and 5(d) have demonstrated essential agreement with the experimental images, the AMR level is chosen to be  $(6D/2^6, 6D/2^7, 6D/2^9)$  such that sufficient accuracy is attained with minimum computing load for all simulation cases. Another issue of concern is the production of unphysically large bubbles at the early stage of droplet coalescence after impact [26]. They are caused by air-cushion effect and have radii about 9–13% of the droplet radius, but triply larger than those observed in the experiments [27–29]. To eliminate the influence of unphysical large bubbles on the internal flow and mass distribution, they are filtered out right after formation [26]. The numerical approach is further validated by comparing simulation results to the other experimental sequences of different outcomes (taken by the b/w high-speed camera, X-StreamTM Vision, XS-4) with corresponding impact conditions. As shown in Figs. 5(e), 5(f), and 6, the evolutions of droplets in all the simulations are very close to that of the experimental images, demonstrating high fidelity of the present numerical methodology.

### B. Mass distribution and flow field inside the merged drops

Based on the full-field simulation, the mass exchange in the separated droplets is calculated to be about 33.4% in the case of rotational separation [Fig. 2(e)]. The transferred mass, however, is about 19.5% in the case of stretching separation [Fig. 2(c)] and 0% in the primary droplets after reflexive separation in a head-on impact. This indicates a much greater amount of mass transfer during the process of rotational separation as compared to those of stretching separation

TABLE I. Physical properties of the liquid (dodecane) and gas (air) for simulations.

Gas viscosity $\mu_g$ (mPa s)	Liquid viscosity $\mu$ (mPa s)	Gas density $\rho_g$ (kg/m <sup>3</sup> )	Liquid density $\rho$ (kg/m <sup>3</sup> )	Surface tension $\sigma$ (mN/m)
0.00168	1.33	1.2	744	24.9

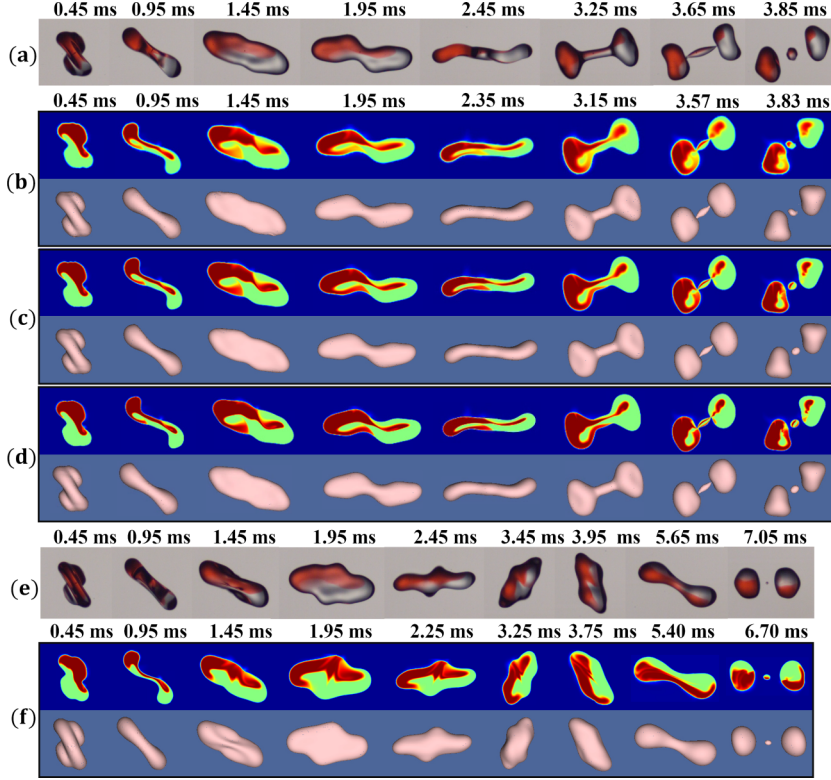


FIG. 5. The sequence of stretching separation ( $We = 35.04$ ,  $B = 0.547$ ) is shown by (a) the experimental images, and the simulation results with (b)  $\Delta_{\min} = 6D/2^8 = D/43$ , (c)  $\Delta_{\min} = 6D/2^9 = D/86$ , and (d)  $\Delta_{\min} = 6D/2^{10} = D/171$ . The sequence of rotational separation ( $We = 35.4$ ,  $B = 0.420$ ) is shown by (e) the experimental images, and (f) the simulation images with  $\Delta_{\min} = 6D/2^9 = D/86$ . In the simulation results, (b)–(d) and (f), the first row shows the tracer distribution at the symmetry plane and the second row presents the 3D surface of the deformed drops.

and reflexive separation. The latter two modes of separations have relatively shorter periods of interactions which are mainly dominated, respectively, by the inertia of SZ and rebounding motions in RI. Comprehension of the distinct characteristics would help prediction and applications of the mixing state between the fluids of droplets at impact [30,31].

To further identify the mechanisms leading to various patterns of separations and collision outcomes with varying  $B$ , numerical simulations are used to comprehend the evolutions of flow fields. Considering the droplet dyed red as shown in Fig. 7, right after impact ( $t = 0.25 T$ ), the mass at SZ (with velocity marked by a dashed arrow) keeps substantial inertia along its original path. But that at RI (with velocity marked by a solid arrow) encounters the impact of its counterpart from the other droplet (dyed white), leading to rebounding flows around the center. A stage similar to that of a flattening disk in the evolution of reflexive separation [Fig. 2(a)] is yielded at  $\sim 0.5 T$  around RI, which is marked off by an ellipse for expression of the oblate (flattening) phase. At  $0.75 T$ , while the velocity vector within the red droplet is inverted at RI, that at SZ follows a rotational motion (around CM) where the liquid is dragged by surface tension. The velocity vectors thus exhibit nearly opposite directions in RI and in SZ, within the same primordial droplet. Consequently, the combined droplets evolve to a four-lobed shape ( $1.0 T$ ), due to the elongation of RI (marked by the ellipse expressing the prolate phase) along with the rotation of SZ. While a similar shape is also illustrated by Ref. [12] for reflexive separation in slightly off-center collision between two droplets,

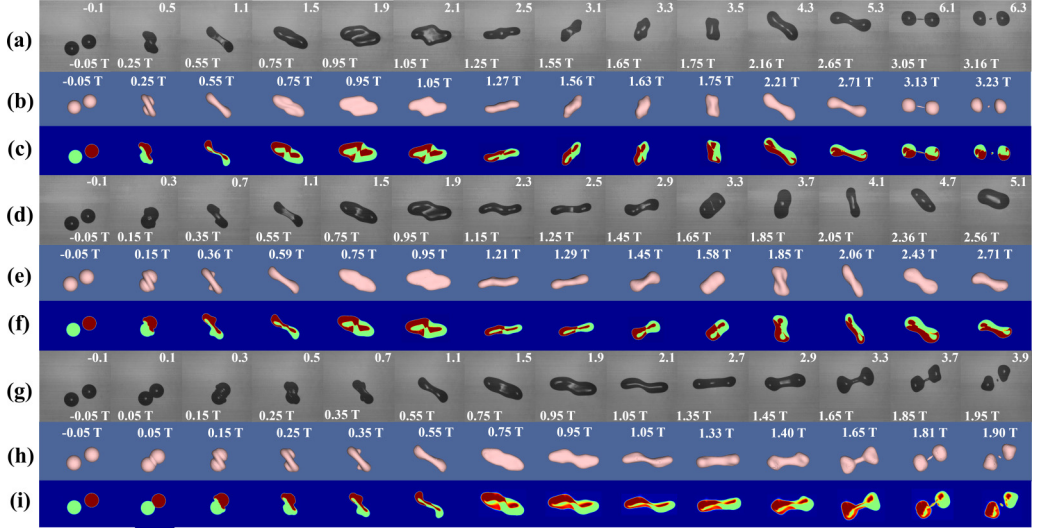


FIG. 6. The sequences of experimental (a), (d), (g) and computational (b), (c), (e), (f), (h), (i) results for dodecane droplets with diameter 0.6 mm. (a), (b), (c)  $We = 35.39$ ,  $B = 0.514$ ; (d), (e), (f)  $We = 35.42$ ,  $B = 0.461$ ; (g), (h), (i)  $We = 35.19$ ,  $B = 0.415$ . (b), (e), (h) present the 3D surfaces of the deformed drops and (c), (f), (i) show the liquid distribution at the symmetry plane. The time in the experiment is measured in the unit of ms while the dimensionless time in the computation is expressed in  $T = \frac{\pi}{4} \sqrt{\frac{\rho D^3}{\sigma}}$ .

the ensuing development on the breakup is prominently different. As shown in Fig. 2(a) for regime IV, the tentatively united droplets separate right during the elongation (prolate phase) that leads to a dumbbell state. In contrast, in rotational separation with significantly larger  $B$ , the rebounding flow does not have sufficient momentum to yield substantial elongation and separation at the first prolate phase, and is then reverted back to the center ( $\sim 1.0$ – $1.25 T$ ).

After recovering to the neutral state, as illustrated by the dashed circle in RI at  $1.25 T$  (Fig. 7), the compression leads to the second time of flattening, i.e., second oblate phase, as symbolized by

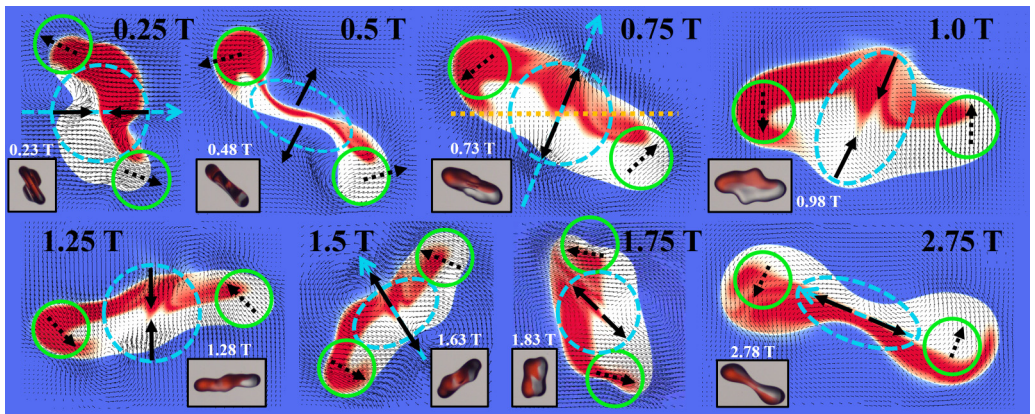


FIG. 7. The simulated evolutions of velocity vectors and merged liquids in a collision leading to rotational separation ( $We = 35.4$ ,  $Oh = 0.0126$ ,  $B = 0.420$ ), where the experimental images are shown for comparisons. The black arrows are used to indicate the approximate velocities of flow motions in RI and in SZ which are marked off by the loops. As a tracking reference for the rotating frame of the united drops in oscillations, a blue dashed arrow expresses the axis of the elongating ellipse around RI at the prolate phases.



the elliptic loop at  $1.5 T$ . After recovering to another neutral state ( $1.75 T$ ), RI starts to elongate again, leading to the second prolate phase ( $\sim 2.0 T$ ) and subsequently a dumbbell shape, before breaking up ( $\sim 2.75 T$ ). As shown by the velocity vectors (approximated by the schematic arrows for illustration) at  $1.5 T$  and  $1.75 T$ , obviously, the rebounding flow of the red droplet tends to flow concurrently in the same direction as the rotating flow, particularly of the white droplet, near the side. The coherent motions of the coupled masses yield further elongation of the united droplet at the second prolate phase. As a consequence of the combined outward motions, a ligament is formed, leading to a dumbbell shape. The neck is eventually ruptured at the moment slightly after  $2.75 T$  when the enhanced momentum overcomes the bonding of surface forces (given by surface tension and viscous drag). As shown by the arrows, the converging masses at the edges tend to rotate around CM while those at the center continue to flow out of the neck zone due to rebounding motions. Accordingly, as revealed from the orthogonal orientations of the velocity vectors at RI and SZ at  $2.75 T$ , centrifugal acceleration is prominently produced. This evolution of flow field demonstrates the significance of rotation and hence centrifugal force on assisting draining of the liquid from the center toward the bulbous sides and eventual disintegration into two primary drops, inside which substantial stirring of masses is observed.

To identify the extent of rotation, one can focus on the colored mass in SZ. As marked by the green tracking loops in Fig. 7 and the dyed part in Figs. 2(d) and 2(e), which moves from the upper right to the lower right, separation occurs after a rotation of nearly  $270^\circ$  [ $\sim 3.13 T$  in Fig. 2(d)]. This is consistent with previous observations of rotations over  $180^\circ$  in off-center collisions [6,8].

### C. Coherence of internal flow motions within a rotating drop with varying impact parameter

The coherent motions emerging in  $\sim 1.5$ – $2.0 T$  are key to determination whether the net inertia of combined internal flows from the different primordial droplets can eventually overcome the restraining surface tension and viscous forces. At  $t = 1.75 T$ , for instance, Fig. 8(c) shows that, in the regime of coalescence as shown in Fig. 2(f) when  $B$  is 0.470, the two streams marked by the solid and dashed arrows at the same side but from RI and SZ, respectively, are not aligned in the concurrent direction. The angle of intersection ( $\psi$ ) is about  $60^\circ$  and is much larger than that of  $B = 0.420$  [Fig. 8(b), showing an included angle  $\psi \approx 29^\circ$ ], which ends in rotational separation as shown in Figs. 2(d) and 2(e). Consequently, the combined flows exhibit weaker coupling and hence less coherence of the rotating and rebounding motions in the direction of elongation (as indicated by the arrows in RI that is marked by the blue dashed circle). The concurrent flow motions are critical in determining whether a favorable flow pattern can be created such that an effective dumbbell geometry of united droplets is formed and results in breakup. The effective net momentum at  $B = 0.470$  is evidently not large enough to overcome the restraining surface forces and lead to separation.

An inverse trend, however, is observed when  $B$  is further reduced, as shown in Fig. 8(a) for  $B = 0.320$  ( $\psi \approx 42^\circ$  at  $t = 1.75 T$ ). It reveals that the coupling between the internal reflective flow and the rotating flow degenerates and cannot yield breakup at the second prolate phase when a dumbbell shape is formed. Similar results of comparisons are observed for other moments mostly in this period (particularly near a critical time that would determine effectiveness of flow coupling, as to be discussed next for modeling). Consequently, a regime of coalescence is formed. It is noted that since the velocity around the center of RI at  $t = 1.55 T$  is very small (near a stagnant state when the flow is about to revert at the oblate phase, which is created also for the other  $B$ 's but in earlier time), the region is not marked with vectors.

From these results, the coupling between the internal reflective flow and the rotating flow from the different impact droplets appears to be maximized at an intermediate  $B$  when RI and SZ both have substantial mass and energy. Though the nonlinear variations and interplays of multiple factors with impact parameters have prevented further quantitative analysis on explication of the breakup, the characteristic behaviors as seen from the respective and united zones of RI and SZ have illustrated the essential difference when  $B$  is changed. This manifests the exclusive existence of rotational



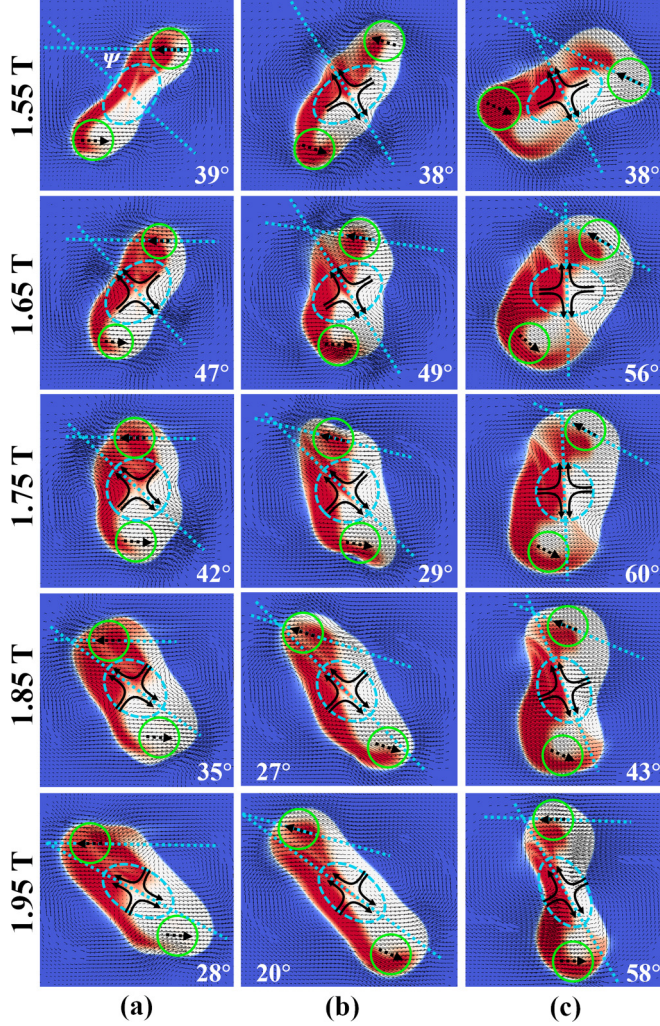


FIG. 8. The distributions of velocity vectors and merged liquids in collisions leading to (a) permanent coalescence ( $B = 0.320$ ,  $We = 34.9$ ), (b) rotational separation ( $B = 0.420$ ,  $We = 35.4$ ), and (c) permanent coalescence ( $B = 0.470$ ,  $We = 35.1$ ). Here the arrows are used to indicate the approximate average velocities of the liquids in the region of interaction (RI, solid arrows) and in the sliding zone at the flank (SZ, dash arrows) which are marked off by the loops.

separation, i.e., regime VI. The regime has characteristics distinctive from the stretching separation (regime V) at higher  $B$  owing to the stretching of masses at SZ and the reflexive separation (regime IV) at smaller  $B$  which is dominated by the rebounding flows in RI.

#### IV. THEORETICAL MODELING FOR VARIOUS TYPES OF DROP SEPARATIONS

Based on the observations of the underlying mechanisms, we have developed a phenomenological model based on a momentum theory including surface tension and viscous effects; this can be used for different types of drop separations. Specifically, respective flow motions in RI and SZ are considered, which lead to a coherent motion at a critical time as observed in the numerical simulations. Here the total momentum of each droplet at the critical time is balanced by the impulse

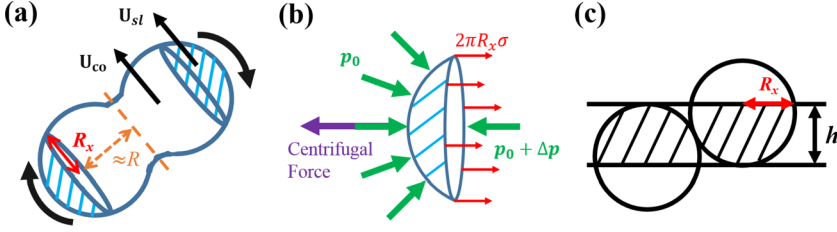


FIG. 9. (a) The typical shape of a rotating drop at the critical time. (b) The free body diagram of the sliding zone. (c) The meaning of  $R_x$  as defined in the schematic of stretching separation model [12].

of surface force and viscous drag before separation can occur [11],

$$P_{\text{cr}} = \int_0^\tau (F_s + F_v) dt' \approx (F_s + F_v) \tau. \quad (1)$$

The critical momentum is the sum of that given by the flows in RI, which exhibit oscillations, and that by the flows in SZ which undergo rotations. Both are treated in the framework of simple harmonic motions in the same plane of projection (as indicated by the orange dashed line in Fig. 7,  $t = 0.75 T$ , which is defined along the original impact orientation),

$$P_{\text{cr}} = \frac{1}{2} |m_{\text{co}} U \cos(\omega_{\text{co}} t_{\text{cr}}) + m_{\text{sl}} U \cos(\omega_{\text{sl}} t_{\text{cr}} + \theta_{\text{sl}})|. \quad (2)$$

Here the mass in RI is  $m_{\text{co}} = \frac{8}{3} \pi \rho \Phi R^3$ , where  $R = D/2$ ,  $\theta_{\text{sl}}$  the empirical phase delay between the flows in RI and SZ (to be determined by the experimental data; see Appendix B), the volumetric fraction  $\Phi = (1 - B)^2 (1 - B^2)^{0.5}$  [12], and the mass in SZ  $m_{\text{sl}} = \frac{8}{3} \pi \rho (1 - \Phi) R^3$ . The oscillating frequency around RI is naturally  $\omega_{\text{co}} = 2\sqrt{\frac{\sigma}{\rho \Phi R^3}}$ . The rotating speed  $\omega_{\text{sl}}$  can be derived from the force balance on the free body of the sliding zone [Fig. 9(b)], which is

$$2\pi R_x \sigma - \left( p_0 + \frac{2\sigma}{R_x} \right) \pi R_x^2 = m_{\text{sl}} R \omega_{\text{sl}}^2 - p_0 \pi R_x^2. \quad (3)$$

Here  $p_0$  is the ambient pressure,  $R_x = \sqrt{R^2 - (R + BD - D)^2}$  can be approximated from the geometry [Fig. 9(c)] of the previous model [12]. By rearranging Eq. (3),  $\omega_{\text{sl}}$  is derived to be

$$\omega_{\text{sl}} = \sqrt{\frac{9\sqrt{B - B^2}\sigma}{8R^3\rho(1 - \Phi)}}. \quad (4)$$

In Eq. (1), the external forces are the restraining surface force,  $F_s \sim \sigma R$ , and the viscous drag,  $F_v \sim \mu U_{\text{sh}} R$ . Here the shearing speed is

$$U_{\text{sh}} = (|\cos(\omega_{\text{co}} t_{\text{cr}})| + |\cos(\omega_{\text{sl}} t_{\text{cr}} + \theta_{\text{sl}})|) U \equiv ZU. \quad (5)$$

The critical time  $t_{\text{cr}}$  is the instant when the net momentum is maximized, which is characterized by the optimum coherence of the flows in RI and SZ as discussed in Sec. III C. This determines whether substantial elongation of the merged drops rotating about CM and subsequent breakup can occur. The time of integration,  $\tau$ , is referred to the period of natural oscillation,  $T$ . This is identical to the characteristic time selected for reflexive separation [32] but different from that used by Ref. [11] for stretching separation,  $R/U_n$ , where  $U_n = UB$ . Equation (1) thus becomes

$$P_{\text{cr}} = \frac{1}{6} \pi \rho D^3 U P = (a\sigma D + c\mu U_{\text{sh}} D) \frac{2T}{\pi}. \quad (6)$$

$P$  is the dimensionless momentum normalized at the critical time, ranging from 0 to 1, and is a function of  $B$ . The empirical coefficients  $a$  and  $c$  can be determined by the least-squares approximation of the experimental data, as described in Appendix B. After rearrangement, the

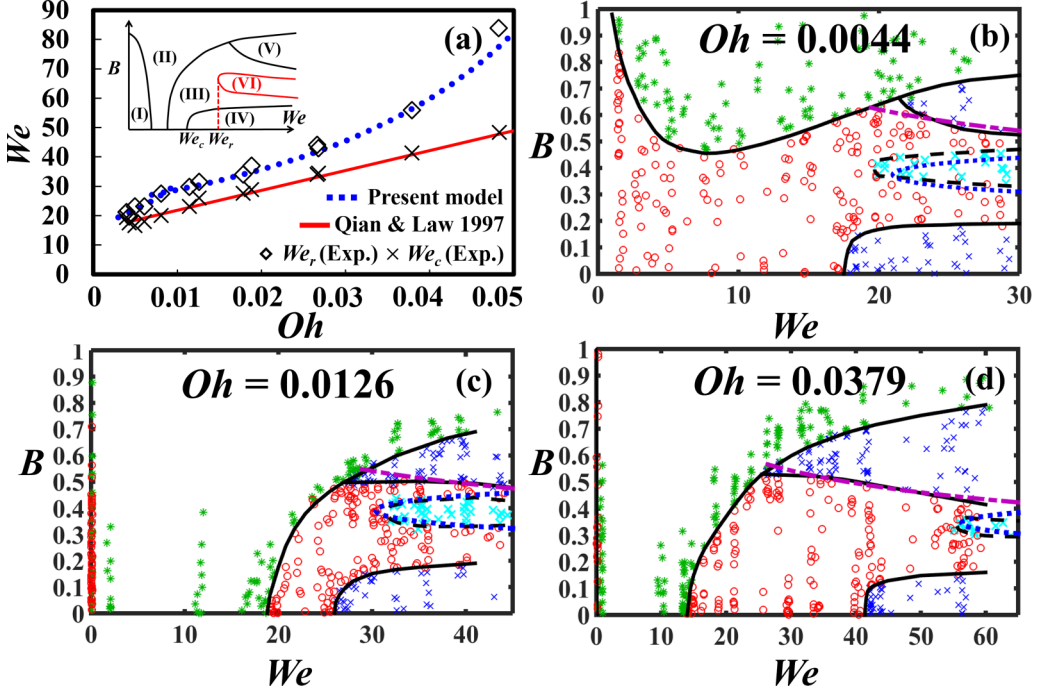


FIG. 10. (a) Experimental measurements of  $We_c$  and  $We_r$ , compared to the model derived by Qian and Law [8] for  $We_c$  and the present model for  $We_r$ . These Weber numbers are defined in the inset, which illustrates the new regime diagram of general liquids. (b)–(d) The regime diagrams of various  $Oh$ 's obtained from the present experiments. Here the boundaries of the rotational separation and stretching separation predicted by the present model are delineated by the dotted blue and dash-dotted purple lines, respectively.

minimum Weber number of transition, or the critical point of regime VI [as indicated in the inset of Fig. 10(a)],  $We_r$ , is obtained:

$$We_r = \left( \frac{3a}{\pi P - 3cZOh} \right)^2, \quad (7)$$

where  $Z = |\cos(\omega_{co}t_{cr})| + |\cos(\omega_{sl}t_{cr} + \theta_{sl})|$ .

To demonstrate the accuracy of the model, various liquids with different diameters have been used to provide the experimental data. As shown in Fig. 10(a), the  $We$ 's at the transition between regime (III) and (IV) at  $B = 0$  for various  $Oh$ 's as measured in present experiments,  $We_c$  (as indicated in the inset), agree well with that predicted by the existing model [8] for reflexive separation. The experimentally measured  $We_r$ 's also coincide with that derived by the present model for rotational separation, thereby justifying the accuracy of the analysis. In contrast to the linearity of  $We_c$ , the scaling of  $We_r$  shows a nonlinear correlation with  $Oh$  and indicates essentially higher magnitude than  $We_c$ . While being still monotonic, the more complicated variations between  $We_r$  and  $Oh$  further reveals the intricate interplays of multiple factors responsible for the creation of rotational separation.

In addition to the critical point, the present model can predict the transitions with varying  $B$ 's and describe the boundaries with moderate accuracy. As shown in Figs. 10(b)–10(d), the width of regime VI is essentially presented by the model, while the measured shape of the regime is not purely symmetric against  $B$  due to uncertainty of the assumptions adopted in the modeling. Furthermore, by changing  $t_{cr}$  and  $\tau$ , as described in Appendix C, the transition boundary of stretching separation

can be predicted with high accuracy as well [see Figs. 10(b)–10(d)]. Therefore, the newly found band of coalescence between (V) and (VI) are clearly described by this model.

## V. CONCLUSION

By scrutinizing the transformations using an improved experimental approach as well as full-field numerical simulations and physical modeling, we have provided a comprehensive elucidation that clarifies the governing mechanisms for various off-center separations of binary droplet collisions. Specifically, in nearly head-on conditions, the creation of separation is dominated by the rebounding flow motions in the center region of interaction. In off-center conditions when the impact parameter is sufficiently large, the stretching mechanics of the masses at the sliding zones of the merged drops determines the onset of separation. In an intermediate region with  $B$  between these two regimes, the coupling of the reflective flows and the rotating part at the sides may lead to coherent motions of united rotational flows that create another regime of separation. Breakup occurs at the second elongation period of the oscillating region of interaction, which is significantly delayed as compared to that of the other two patterns of separations. Variations of these regimes can be identified clearly in terms of the generalized 3D diagram expressed by the Ohnesorge number and the Weber number with varying impact parameters.

It is noted that, the ambiguity and dissension on differentiation of the dominating mechanisms for off-center separations as seen in the literature could be related to the high sensitivity of various events near the transitions. Furthermore, the variation of  $Oh$  can change the scope of rotational separation such that its formation is not easily detected. To enhance resolution and reduce dispersion of data points around the transition boundaries, the precision for determining the parametric conditions of off-center collisions has been increased by taking a great number of data points with utilization of two cameras in parallel; this ensures coincidence of the collision plane with the imaging plane. Moreover, different liquids and droplet sizes have been tested and the regime diagram is presented in a generalized way based on the key dimensionless variables ( $We$ ,  $Oh$ , and  $B$ ) in the range available in the experiments. By using the VOF numerical simulations, it is the first time that the transitions of permanent coalescence, rotational separation and stretching separation can be accurately produced, to the authors' knowledge. The evolution of flow field within the merged drops thus provides explicit elucidation of the scenarios regarding the onset of breakup after impact when  $B$  is varied. In contrast to the straightforward processes of reflexive separation and stretching separation that can be understood explicitly, rotational separation involves much more complexity due to interplays among multiple factors varying with  $B$  in the intermediate range. The newly observed coupling between the flows at the region of interaction and sliding zones is hence considered in the model, which could be generalized for different types of drop separations. The agreement of the modeling results with previous and the present experimental data thus verifies the reasonability of the assumptions and interpretations for the underlying structures.

Comprehension of the mechanisms dominating at different impact angles would help analysis of various outcomes in collisions between soft bodies of similarity. Not only in related fluid dynamic researches, immediate significance could be seen in extensive fields including nuclear fusion-fission processes [16,19] based on a nuclear liquid-drop model. Another example is the impacts between astrophysical bodies [21] such as planets and stars where rotational motions and centrifugal forces play a critical role in the evolutions, specifically regarding redistributions of the mass, momentum and energy.

## ACKNOWLEDGMENTS

The work is supported by the Ministry of Science and Technology of Taiwan (Grant No. MOST 102-2221-E-002-064-MY3) and National Taiwan University (Grants No. NTU-CDP-106R7822, NTU-107L7822, and NTU-108L7822). We thank the National Center for High-performance



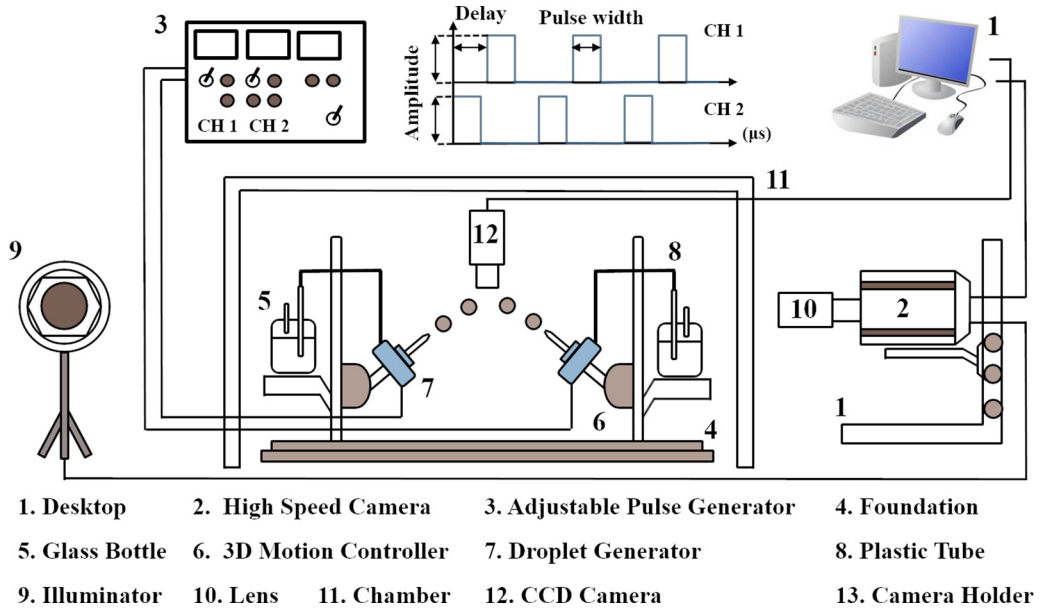


FIG. 11. Schematic of the experiment setup.

Computing for computer time and facilities. We are grateful of Prof. J. T. Yang's support on a color high-speed camera.

#### APPENDIX A: EXPERIMENTAL METHODOLOGY

The experimental setup is shown in Fig. 11, similar to that in Ref. [23]. Two identical droplets made of decane, dodecane, tetradecane, hexadecane, silicone oil (KF-96L-5cs, Shin-Etsu Chemical Co., Ltd.), and water, respectively, were generated from two glass nozzles by the vibrations of piezoelectric plates. To identify the mass distribution in binary droplet impact, one of the paired droplets was doped with a small amount of dye additive, Sudan Red, which made negligible change in the fluid properties (within 0.4%). Via an electronic control circuit, the velocity and radius of droplets can be adjusted by controlling the amplitude and pulse width of the electronic signal. Time-resolved images were recorded by high-speed CMOS digital cameras (in black/white,

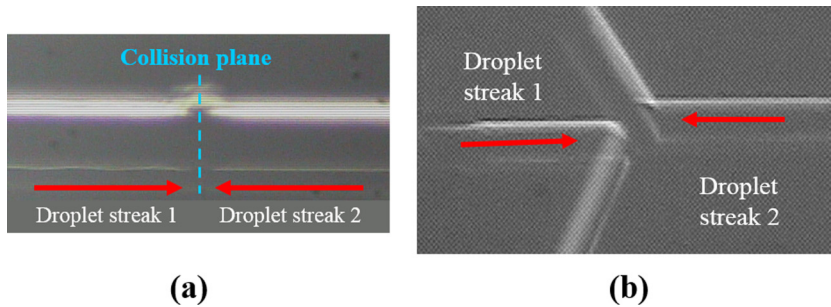


FIG. 12. Top views of the colliding droplet streaks (exposure time: 1/60 s) which (a) appear collinear if the collisions are made in the same plane and (b) are bent if not in the same collision plane.



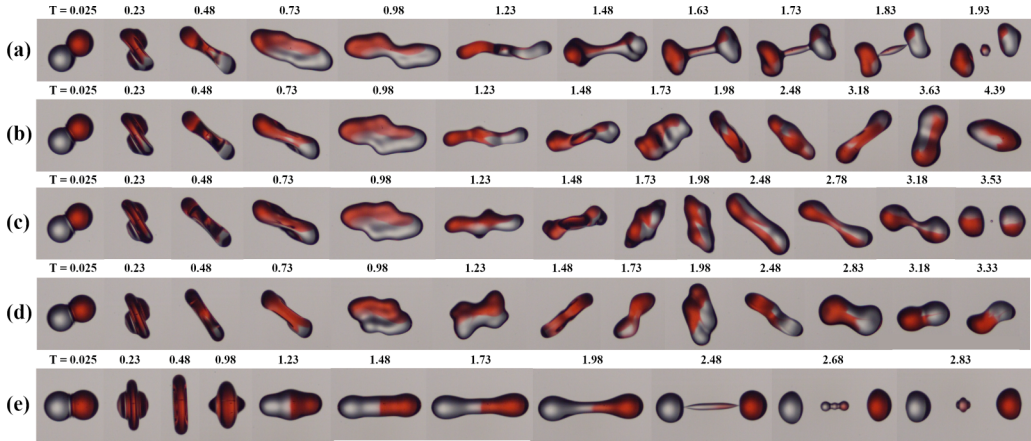


FIG. 13. The experimental sequences of impinging dodecane droplets with decreasing  $B$  at similar  $We$ 's of (a) stretching separation ( $We = 35.04$ ,  $B = 0.547$ ), (b) coalescence ( $We = 35.13$ ,  $B = 0.470$ ), (c) rotational separation ( $We = 35.44$ ,  $B = 0.420$ ), (d) coalescence ( $We = 34.90$ ,  $B = 0.320$ ), and (e) reflexive separation ( $We = 33.60$ ,  $B = 0.002$ ). Here the dimensionless time is expressed in the unit of  $T$  (cf. Fig. 2).

X-Stream<sup>TM</sup> Vision, XS-4, and in color, Vision Research, Phantom V310), which supported a resolution of  $512 \times 512$  pixels with 5000–10000 frames per second (fps). The shutter of the high-speed camera was synchronized with a LED lamp while recording the images, and the exposure time of shutter can be set down to  $1 \mu s$  to avoid blurring due to background scattering. Moreover, to ensure that the collision events occurred on the same focal plane as that of visualization, a CCD camera was used on top to monitor the impacts of two droplet streams, as shown in Fig. 12. It is seen from the top view that when the collisions are made in the same plane, the two streams of droplets exhibit a collinear path, whereas they appear to be bent away if not in the same plane. Based on the experimental setup, sequential images of droplet collisions with  $B = 0.0$ – $0.9$  can be captured by the camera viewing from the side and analyzed for the relative velocities on the

TABLE II. Properties of tested liquids (25 °C).

	Density (kg/m <sup>3</sup> )	Viscosity (mPa·s)	Surface tension (mN/m)	Diameter ( $\mu$ m)	100 Oh
Decane	731	0.82	23.4	300	1.14
				600	0.81
Dodecane	744	1.33	24.9	300	1.78
				600	1.26
Tetradecane	759	2.05	26.0	300	2.66
				600	1.88
Hexadecane	773	3.0	27.0	300	3.79
				600	2.68
Water	996	0.92	72.0	300	0.63
				450	0.51
				600	0.44
				700	0.41
Silicone oil (KF-96L-5cs)	924	4.25	18.6	300	5.92
				450	4.83

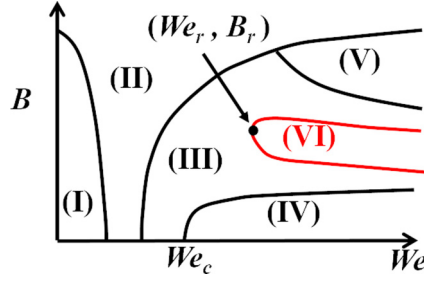


FIG. 14. The definitions of  $B_r$  and  $We_r$  indicating the critical point of rotational separation on the regime diagram.

collision plane. The typical collision outcomes are shown in Fig. 13. By using the high-speed photography, the sequences of droplet collision events from high to low impact parameters can be clearly resolved while keeping a similar  $We$ , as shown in Fig. 13. The surface tensions of tested liquids were measured by a tensiometer (DCAT, DataPhysics Instruments GmbH) with accuracy of  $\pm 0.05$  mN/m, and viscosity by a rheometer (Brookfield DV3T, AMETEK, Inc.) with accuracy of  $\pm 0.01$  mPa s. The fluid properties are listed in Table II.

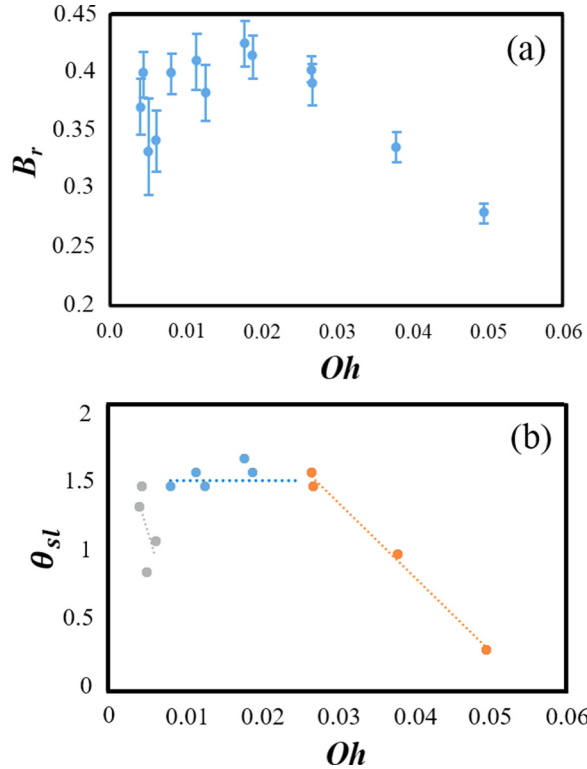


FIG. 15. The relations of (a)  $B_r$  versus  $Oh$  measured experimentally and marked by error bars, and (b)  $\theta_{sl}$  versus  $Oh$  fitted from (a) via the procedure as mentioned.

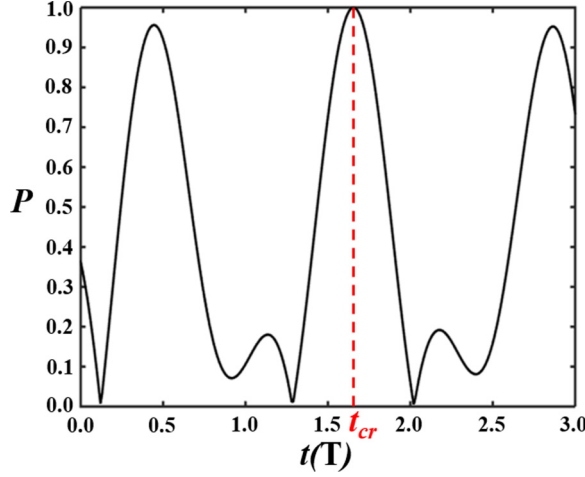


FIG. 16. An example of  $P$  varying with  $t$  (in the unit of  $T$ ) at  $B = 0.39$  and  $Oh = 0.0126$ .

## APPENDIX B: FITTING PARAMETERS IN THE MODEL

Due to the complexity in modeling the process of rotational separation as seen, there are three parameters to be fitted, i.e.,  $a$ ,  $c$ , and  $\theta_{sl}$ . In the fitting process, firstly the empirical phase delay  $\theta_{sl}$ , which is closely related to the impact parameter when coherence of the flows in RI and SZ may occur, is obtained from the experimental data ( $Oh$ ,  $B_r$ ) for a set of ( $a$ ,  $c$ ). The coefficients ( $a$ ,  $c$ ) refer to the weightings of surface tension and viscous forces, respectively, and are mainly correlated with  $We_r$ , hence relegated to the next step of fitting procedure. Here  $B_r$  is defined in Fig. 14 and its quantities measured with various  $Oh$ 's are plotted in Fig. 15(a) with error bars. The procedure of fitting  $\theta_{sl}$  is described in the following.

(1) Find the time ( $t_{cr}$ ) where  $P$  [Eq. (6)] is maximized with an arbitrary value of  $\theta_{sl}$  ( $0-\pi$ ), as shown in Fig. 16, which corresponds to the second oscillation period when coherence of the flows in RI and SZ can form as observed in the simulation and experimental results.

(2) Input a fixed set of ( $a$ ,  $c$ ),  $t_{cr}$  and  $[\theta_{sl}(i), B(j)] = [0-2\pi, 0.25-0.45]$  into Eq. (7) and obtain  $We[\theta_{sl}(i), B(j)] = \begin{Bmatrix} We[\theta_{sl}(1), B(1)] & \cdots & We[\theta_{sl}(1), B(j)] \\ \vdots & & \vdots \\ We[\theta_{sl}(i), B(1)] & \cdots & We[\theta_{sl}(i), B(j)] \end{Bmatrix}$ , where the values of ( $a$ ,  $c$ ) do not influence  $\theta_{sl}$ . To note, the range of  $B(j)$  of the critical point is selected from 0.25 to 0.45 according to the experimental observations for all the events of rotational separations.

(3) Obtain (  $\begin{matrix} \vdots \\ \text{minimum}\{We[\theta_{sl}(1), B(j)]\} \end{matrix}$  ) and the corresponding [  $\begin{matrix} \vdots \\ B(1)_{at \theta_{sl}(1)} \end{matrix}$  ].

(4) Calculate the minimum of {  $\begin{matrix} \vdots \\ [B_r - B(i)_{at \theta_{sl}(i)}]^2 \end{matrix}$  } and obtain the corresponding  $\theta_{sl}$ .

TABLE III. The values of  $\theta_{sl}$  fitted for different ranges of  $Oh$ .

	$Oh < 0.007$	$0.007 < Oh < 0.025$	$Oh > 0.025$
$\theta_{sl}$	$-178.9 Oh + 2.1$	1.54	$-54.4 Oh + 3.0$

TABLE IV. The values of  $a$  and  $c$  fitted for different ranges of  $Oh$ .

	$Oh < 0.007$	$0.007 < Oh < 0.025$	$Oh > 0.025$
$(a, c)$	$a = 8.5, c = 28.0$	$a = 10.2, c = 9.7$	$a = 10.2, c = 9.7$

(5) Input this  $\theta_{sl}$  back to step (1) and repeat the process till the value of  $\theta_{sl}$  reaches convergence, i.e., when the absolute difference of  $\theta_{sl}$  between the last two rounds is smaller than a prescribed value.

Based on the process, the experimentally measured values of  $B_r$  can be used for fitting  $\theta_{sl}$  per se.

The results are shown in Fig. 15(b) and the fitting values of  $\theta_{sl}$  are listed in Table III. In view of the variation of measured relation of  $B_r$  versus  $Oh$  (obtained by different liquids), as seen Fig. 15(a),  $\theta_{sl}$  is fitted against  $Oh$  in three ranges so as to achieve higher conformity [Fig. 15(b)]. It is noted that, for the lowest range,  $Oh < 0.007$ , only water has been used.

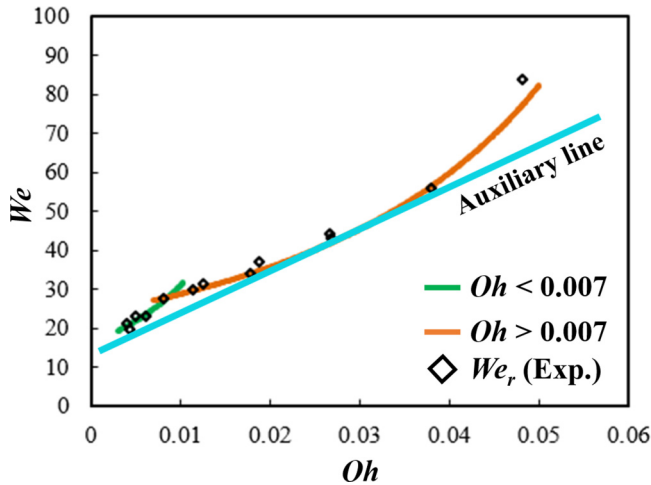
Based on the values of  $\theta_{sl}$ ,  $(a, c)$  can be further iterated to render the least squares of deviations from measured  $We_r$ . The results are shown in Table IV. Since the values of  $(a, c)$  in the ranges of  $0.007 < Oh < 0.025$  and  $Oh > 0.025$  are the same, two, instead of three, regression lines for predicting  $We_r$  are obtained, as shown in Fig. 17 [also in Fig. 10(a)].

#### APPENDIX C: THE PRESENT MODEL FOR STRETCHING SEPARATION

For stretching separation, the time of integration,  $\tau$ , in Eq. (1) is taken as  $D/U$  [11], and the coefficients  $a$  and  $c$  are altered to  $a_{st}$  and  $c_{st}$ , respectively. Since the rotational motion of the interaction region is insignificant and the phase angle of the sliding zones varies negligibly,  $\theta_{sl}$  is set to zero. In addition,  $t_{cr}$  in Eq. (2) is assumed to be a constant since the sliding zones dominate the stretching separation. After rearrangement of Eqs. (1) and (6) with the altered parameters, the transition boundary of the stretching separation is derived as

$$We = \left( \frac{3c_{st}ZOh + \sqrt{9(c_{st}ZOh)^2 + 12\pi Pa_{st}}}{2\pi P} \right)^2. \quad (C1)$$

Here the empirical parameters  $a_{st} = 24$ ,  $c_{st} = 1$ , and  $t_{cr} = 0.32$ , which are obtained by the least-squares method.


 FIG. 17. The regression results of Eq. (7) for  $We_r$ .

- [1] R. Gunn, Coalescence and separation in binary collisions of liquid drops, *Science* **150**, 695 (1965).
- [2] L. G. Moretto, K. Tso, N. Colonna, and G. J. Wozniak, New Rayleigh-Taylor–Like Surface Instability and Nuclear Multifragmentation, *Phys. Rev. Lett.* **69**, 1884 (1992).
- [3] W. Bauer, G. F. Bertsch, and H. Schulz, Bubble and Ring Formation in Nuclear Fragmentation, *Phys. Rev. Lett.* **69**, 1888 (1992).
- [4] H. H. Chiu, Advances and challenges in droplet and spray combustion. I. Toward a unified theory of droplet aerothermochemistry, *Prog. Energy Combust. Sci.* **26**, 381 (2000).
- [5] G. Grant, J. Brenton, and D. Drysdale, Fire suppression by water sprays, *Prog. Energy Combust. Sci.* **26**, 79 (2000).
- [6] W. Park, Behavior of water drops colliding in humid nitrogen. Ph.D. thesis, Department of Chemical Engineering, The University of Wisconsin (1970).
- [7] K. L. Pan, P. C. Chou, and Y. J. Tseng, Binary droplet collision at high Weber number, *Phys. Rev. E* **80**, 036301 (2009).
- [8] J. Qian and C. K. Law, Regimes of coalescence and separation in droplet collision, *J. Fluid Mech.* **331**, 59 (1997).
- [9] P. R. Brazier-Smith, S. G. Jennings, and J. Latham, The interaction of falling water drops: coalescence, *Proc. R. Soc. Lond. A* **326**, 393 (1972).
- [10] V. A. Arkhipov, I. M. Vasenin, and V. F. Trofimov, Stability of colliding drops of ideal liquid, *J. Appl. Mech. Tech. Phys.* **24**, 371 (1983).
- [11] Y. J. Jiang, A. Umemura, and C. K. Law, An experimental investigation on the collision behavior of hydrocarbon droplets, *J. Fluid Mech.* **234**, 171 (1992).
- [12] N. Ashgriz and J. Y. Poo, Coalescence and separation in binary collisions of liquid drops, *J. Fluid Mech.* **221**, 183 (1990).
- [13] M. Orme, Experiments on droplet collisions, bounce, coalescence and disruption, *Progr. Energy Combust. Sci.* **23**, 65 (1997).
- [14] G. H. Ko and H. S. Ryou, Modeling of droplet collision-induced breakup process, *Int. J. Multiphase Flow* **31**, 723 (2005).
- [15] C. Gotaas, P. Havelka, H. A. Jakobsen, H. F. Svendsen, M. Hase, N. Roth, and B. Weigand, Effect of viscosity on droplet-droplet collision outcome: Experimental study and numerical comparison, *Phys. Fluids* **19**, 102106 (2007).
- [16] A. Menchaca-Rocha, A. Cuevas, M. Chapa, and M. Silva, Rotating-liquid-drop model limit tested on macroscopic drops, *Phys. Rev. E* **47**, 1433 (1993).
- [17] S. Popinet, Gerris: A tree-based adaptive solver for the incompressible Euler equations in complex geometries, *J. Comput. Phys.* **190**, 572 (2003).
- [18] T. Inamuro, T. Ogata, S. Tajima, and N. Konishi, A lattice Boltzmann method for incompressible two-phase flows with large density differences, *J. Comput. Phys.* **198**, 628 (2004).
- [19] H. J. Krappe and K. Pomorski, *Theory of Nuclear Fission: A Textbook* (Springer Science & Business Media, Berlin, 2012).
- [20] A. Mazloomi Moqaddam, S. S. Chikatamarla, and I. V. Karlin, Simulation of binary droplet collisions with the entropic lattice Boltzmann method, *Phys. Fluids* **28**, 022106 (2016).
- [21] F. D. Becchetti, S. L. Mark, W. R. Robinson, and M. Ojaruega, Colliding nuclei to colliding galaxies: Illustrations using a simple colliding liquid-drop apparatus, *Am. J. Phys.* **83**, 846 (2015).
- [22] G. Finotello, J. T. Padding, N. G. Deen, A. Jongsma, F. Innings, and J. A. M. Kuipers, Effect of viscosity on droplet-droplet collisional interaction, *Phys. Fluids* **29**, 067102 (2017).
- [23] K. L. Pan, Y. H. Chen, J. C. Chen, K. L. Huang, C. H. Wang, and M. C. Lai, Controlling droplet bouncing and coalescence with surfactant, *J. Fluid Mech.* **799**, 603 (2016).
- [24] C. Tang, P. Zhang, and C. K. Law, Bouncing, coalescence, and separation in head-on collision of unequal-size droplets, *Phys. Fluids* **24**, 022101 (2012).
- [25] See Supplemental Material at <http://link.aps.org/supplemental/10.1103/PhysRevFluids.4.123602> for supplemental movies.
- [26] C. Tang, J. Zhao, P. Zhang, C. K. Law, and Z. Huang, Dynamics of internal jets in the merging of two droplets of unequal sizes, *J. Fluid Mech.* **795**, 671 (2016).



- [27] S. T. Thoroddsen, T. G. Etoh, and K. Takehara, Air entrapment under an impacting drop, *J. Fluid Mech.* **478**, 125 (2003).
- [28] W. Bouwhuis, R. C. A. van der Veen, T. Tran, D. L. Keji, K. G. Winkels, I. R. Peters, D. van der Meer, C. Sun, J. H. Snoeijer, and D. Lohse, Maximal Air Bubble Entrainment at Liquid-Drop Impact, *Phys. Rev. Lett.* **109**, 264501 (2012).
- [29] D. L. Keji, K. G. Winkels, M. R. Castelijns, and J. H. Snoeijer, Bubble formation during the collision of a sessile drop with a meniscus, *Phys. Fluids* **25**, 082005 (2013).
- [30] D. Zhang, P. Zhang, Y. Yuan, and T. Zhang, Hypergolic ignition by head-on collision of N, N, N', N' – tetramethylethylenediamine and white fuming nitric acid droplets, *Combust. Flame* **173**, 276 (2016).
- [31] K. Sun, P. Zhang, M. Jia, and T. Wang, Collision-induced jet-like mixing for droplets of unequal-sizes, *Int. J. Heat Mass Transf.* **120**, 218 (2018).
- [32] C. Planchette, H. Hinterbichler, M. Liu, D. Bothe, and G. Brenn, Colliding drops as coalescing and fragmenting liquid springs, *J. Fluid Mech.* **814**, 277 (2017).